

Probing the baryogenesis and dark matter relaxed in phase transition by gravitational waves and colliders

Fa Peng Huang^{1,*} and Chong Sheng Li^{2,3}

¹*Center for Theoretical Physics of the Universe, Institute for Basic Science (IBS), Daejeon 34051, Korea*

²*Department of Physics and State Key Laboratory of Nuclear Physics and Technology, Peking University, Beijing 100871, China*

³*Center for High Energy Physics, Peking University, Beijing 100871, China*
(Received 11 October 2017; published 27 November 2017)

The cosmological phase transition with Q-balls production mechanism can explain the baryogenesis and dark matter simultaneously, where constraints on dark matter masses and reverse dilution are significantly relaxed. We study how to probe this scenario by collider signals at QCD next-to-leading order and gravitational wave signals.

DOI: [10.1103/PhysRevD.96.095028](https://doi.org/10.1103/PhysRevD.96.095028)

I. INTRODUCTION

A longstanding issue in cosmology and particle physics is understanding the nature of dark matter (DM) and the origin of baryon asymmetry of the universe (BAU), which is quantified by $\eta_B \equiv n_B/s \sim 10^{-10}$ [1,2] from the experiment's data of the big bang nucleosynthesis. To produce the observed BAU, the well-known Sakharov conditions for successful baryogenesis (baryon number violation, C and CP violation, and departure from equilibrium dynamics or CPT violation) [3] are necessary. There are various baryogenesis mechanisms [4] to provide these three conditions, such as grand unified theory baryogenesis, Affleck-Dine baryogenesis, electro-weak baryogenesis, leptogenesis, and so on. On the other hand, the absence of DM signal in DM direct detection experiments may give us a hint that there may be some new approaches to probe the DM, such as gravitational wave (GW) experiments. In this work, we try to use the GWs and collider signals to probe the baryogenesis mechanism, which can explain the BAU and DM simultaneously and associates a strong first-order phase transition (FOPT) [5] at several TeV scale with Q-balls [6–8] generation to relax the constraints. Most of the mechanisms to simultaneously solve the baryogenesis and DM puzzles usually have two strong constraints, which are systemically discussed in Ref. [9]. One constraint is that the DM mass is usually several GeV, and the other constraint is that in most cases the baryon asymmetry produced by heavy particle decays in the early Universe should not be destroyed by inverse washout processes. In order to guarantee the efficiency production of the baryon asymmetry from heavy particle decay, we need to tune the reheating temperature carefully. A strong FOPT with Q-balls production can be used to relax the two constraints [5], since the mass of the DM candidate can be larger than TeV in the symmetry broken phase due to the strong FOPT [9] and the strong FOPT-induced Q-balls can quickly packet the DM

candidates into the Q-balls to greatly reduce the inverse dilution [5]. In this phase transition scenario, phase transition GWs are produced during the strong FOPT, which may provide a new approach to probe the new physics beyond the standard model (SM) after the discovery of GWs by aLIGO [10]. Constraints from the current LHC data [11], and predictions at future LHC will be studied in detail in this paper. The signals and backgrounds with QCD next-to-leading order (NLO) accuracy are also investigated in this work. GW signals and collider signals will provide a realistic and complementary test on this scenario.

In Sec. II, we describe the effective Lagrangian in the framework of effective field theory (EFT), and show that the effective operators can explain the BAU and the DM simultaneously. In Sec. III, we discuss concrete realization of the FOPT relaxed mechanism and calculate the phase transition GW signals in the parameter spaces allowed by the observed BAU and the DM energy density. In Sec. IV, the constraints and predictions at the LHC are discussed in detail. Section V contains our final conclusions.

II. THE SIMPLIFIED SCENARIO FOR BARYOGENESIS AND DARK MATTER

In order to explain the baryogenesis and DM simultaneously in this work, the EFT approach is adopted to provide the model independent predictions at hadron colliders and GW detectors. First, our discussions are based on the following simplified Lagrangian [5,12],

$$\begin{aligned} \mathcal{L} = & \frac{1}{2}(\partial_\mu S)^2 - U(S) + (\partial_\mu \chi)^*(\partial_\mu \chi) - k_1^2 S^2 \chi^* \chi \\ & - \sum_i \frac{h_i^2}{2} S^2 \phi_i^2 + \sum_i \frac{1}{2} (\partial_\mu \phi_i)^2 \\ & - \sum_{a=1,2} \frac{\lambda_a^{ijk}}{\Lambda^2} \bar{X}_a P_R D_i \bar{U}_j^c P_R D_k + \frac{\zeta_a}{\Lambda} \bar{X}_a Y^c \chi \chi^* \\ & + \text{H.c.} \end{aligned} \quad (1)$$

*huangfp@ibs.re.kr

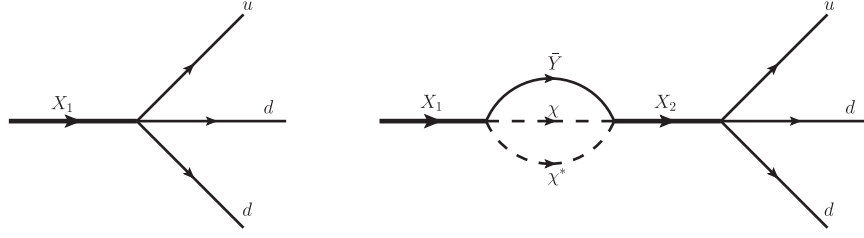


FIG. 1. Schematic Feynman diagrams for the production of BAU from the interference effects between tree-level diagram and the two-loop diagram.

with $U(S) = \lambda_S(S^2 - \sigma^2)^2/4$. And X_a represents heavy Dirac fermionic mediators with several TeV mass, where $a = 1, 2$ and we assume $m_{X_2} > m_{X_1}$. The couplings λ_a^{ijk} and ζ_a are complex numbers, which provide the CP violation source. X_a connects the visible quarks sector and the hidden sector. U and D represent the up-type quark and down-type quark, respectively. The dimension-six operator $\frac{\lambda_a^{ijk}}{\Lambda^2} \bar{X}_a P_R D_i \bar{U}_j^C P_R D_k$ plays important roles in this scenario and appears in many baryogenesis mechanisms, such as the famous hylogenesis mechanism firstly proposed in Ref. [12]. Collider signals induced by this dimension-six operator have been studied at tree level using LHC Run-I data in Ref. [11]. S is a real scalar field, which is the order parameter field for the strong FOPT. And χ is a complex field with a global $U(1)$ symmetry. ϕ_i is some unspecified real scalar field, which helps to enhance the strength of the phase transition. The effective Lagrangian should be realized in some renormalizable UV-completed models, which are left for our future studies.

At the very early Universe, the potential $U(S)$ is symmetric due to thermal effects. At this state, the S field has no vacuum expectation value (VEV); thus the particles χ , Y , and ϕ_i are massless at tree level. At a certain time, the nonthermal decays of X_1 and \bar{X}_1 occur, which produce baryon asymmetry. The decay width of the dominant channel for X_1 at tree level $X_1 \rightarrow \bar{Y}\chi\chi^*$ is

$$\Gamma(X_1 \rightarrow \bar{Y}\chi\chi^*) = \frac{|\zeta_1|^2 m_{X_1}^3}{1024\pi^3 \Lambda^2}. \quad (2)$$

Another important decay channel is $X_1 \rightarrow udd$ if only the first generation is considered as an example. Thus, the corresponding decay width at tree level can be written as

$$\Gamma(X_1 \rightarrow udd) = \frac{3|\lambda_1|^2 m_{X_1}^5}{1024\pi^3 \Lambda^4}. \quad (3)$$

As shown in Fig. 1, the interference effects between the two-loop diagram and the tree-level diagram produce net baryon asymmetry for per one (X_1, \bar{X}_1) pair decay, which can be quantified as

$$\begin{aligned} \varepsilon &\equiv \frac{1}{2\Gamma_{X_1}} (\Gamma(X_1 \rightarrow udd) - \Gamma(\bar{X}_1 \rightarrow \bar{u}\bar{d}\bar{d})) \\ &\sim 10^{-5} \times \frac{\text{Im}[\lambda_1^* \lambda_2 \zeta_1 \zeta_2^*] m_{X_1}}{|\zeta_1|^2 m_{X_2}} \left(\frac{m_{X_1}}{\Lambda}\right)^4. \end{aligned} \quad (4)$$

Essentially, we have $\varepsilon \propto \text{Im}[\lambda_1^* \lambda_2 \zeta_1 \zeta_2^*]$, which represents the tree-loop interference effects [11,12]. Once the asymmetry factor is obtained, the produced BAU can be expressed as $\eta_B \equiv n_B/s \sim \varepsilon/g_*$. To satisfy the observed BAU $\eta_B \approx 10^{-10}$, $\varepsilon \sim 10^{-8}$ is needed for $g_* \sim 10^2$. Then, the allowed parameter spaces can be obtained from Eq. (4) by requiring $\varepsilon \sim 10^{-8}$ for a successful baryogenesis mechanism. The allowed parameter spaces for producing the observed BAU are shown as the colorful surface in Fig. 2, where we have $\Lambda > m_{X_2} > m_{X_1}$ for the consistence of the EFT. We can see that there are no strong constraints on the absolute values of the model parameters as long as the three ratio values $(\frac{\text{Im}[\lambda_1^* \lambda_2 \zeta_1 \zeta_2^*]}{|\zeta_1|^2}, \frac{m_{X_1}}{m_{X_2}}, \frac{m_{X_1}}{\Lambda})$ satisfy a certain relation in Eq. (4).

In this scenario, we have $n_\chi = n_{\chi^*} = n_Y = n_B$ after the decay of X_a particles from baryon number conservation. With the production of BAU, the DM candidate can also be given. In most mechanisms (we take the hylogenesis mechanism proposed in Ref. [12] as a typical example)

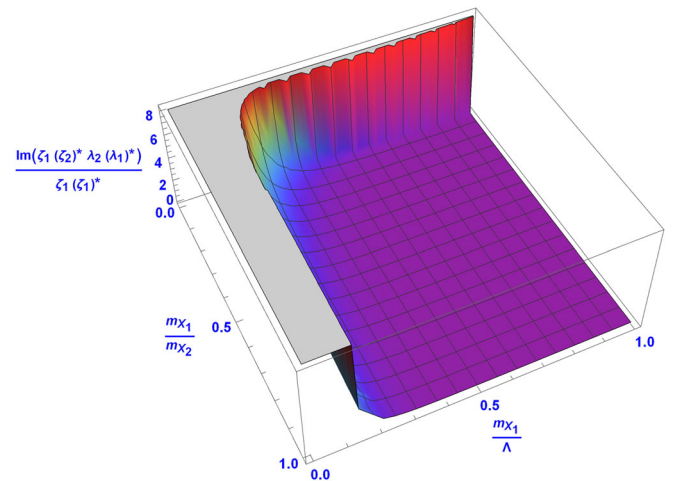


FIG. 2. Parameter spaces for producing the observed BAU. The parameter spaces on the colored surface are allowed.

for explaining DM and BAU simultaneously, the DM masses should be several GeV [11,12]. And the rescatter effects can wash out the generated baryon asymmetry in the decays of the X_1, \bar{X}_1 pair. To suppress this inverse process, additional strong constraints are needed, such as the requirements of tuning the reheating temperature [11,12]. These two constraints can greatly suppress the allowed parameter spaces for successful baryogenesis and DM. A phase transition mechanism [9] with Q-balls generation [5] is studied in this work to avoid these constraints, which are discussed carefully in the following section.

III. STRONG FIRST-ORDER PHASE TRANSITION AT TEV SCALE AND GRAVITATIONAL WAVE SIGNALS

First, we qualitatively describe the scenario that the phase transition with Q-balls generation can relax the above constraints. After the production of baryon asymmetry from heavy particle decay, we assume that a strong FOPT occurs at several TeV scale by the S field in Eq. (1). Thus, the S field acquires VEV, and the χ particle obtains large mass. By assuming that the χ particle mass in the broken phase is much larger than the critical temperature, namely, $m_\chi = k_1\sigma \gg T_c$, χ particles get trapped in the remnants of the old phase. Under the assumption $m_\chi = k_1\sigma \gg T_c$, the χ particle numbers entered into the symmetry breaking phase are negligibly small due to the exponential suppression $e^{-k_1\sigma/T_c}$. And with the bubble expansion, they eventually shrink to very small size objects and become the so-called Q-balls as DM candidates. As for the particle Y , it enters into the symmetry breaking phase and remains massless. Thus, its contribution to the DM energy density is negligible and we leave the study of its roles in the early Universe for our future study. Particles ϕ_i also obtain certain mass $m_\phi = h_i\sigma$. By requiring the condition $T_c \gtrsim h_i\sigma, m_S$, particles S and ϕ_i can make efficient thermal contributions to the strong FOPT. More explicitly, even when $3T_c > h_i\sigma, m_S$, they can still make some thermal contribution to the FOPT. Thus, the fundamental requirement for this scenario can be written as

$$k_1\sigma \gg T_c \gtrsim h_i\sigma, m_S. \quad (5)$$

Now, we begin the quantitative investigation from the conditions for a strong FOPT. From Eq. (1), using the standard finite temperature quantum field theory [13], we can obtain the following one-loop effective potential at finite temperature,

$$V_{\text{eff}}(S, T) \approx \frac{(-\mu_S^2 + cT^2)S^2}{2} - \frac{eT(S^2)^{3/2}}{12\pi} + \frac{\lambda_S}{4}S^4, \quad (6)$$

where $\mu_S^2 = \lambda_S\sigma^2$ and $m_S^2 = 2\lambda_S\sigma^2$. The parameter e quantifies the interactions between the S field and the bosons,

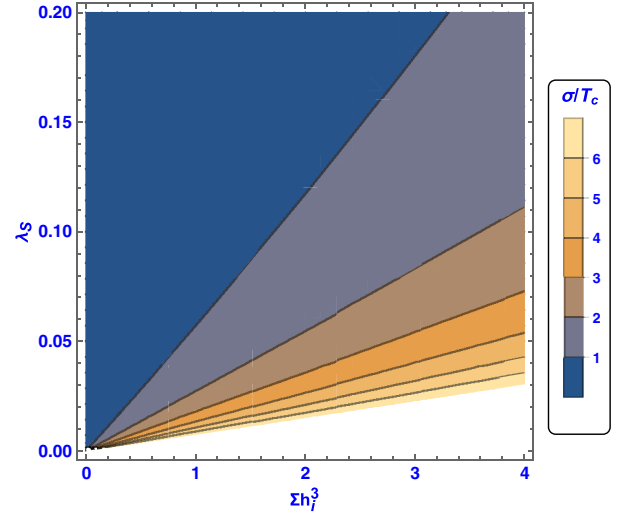


FIG. 3. Parameter spaces for producing a strong FOPT where the blue region is excluded.

which can make thermal contributions to the phase transition. Here, the high temperature expansion approximation (namely, the thermal boson function $J_{\text{boson}} = -\frac{\pi^4}{45} + \frac{\pi^2 m^2}{12 T^2} - \frac{\pi}{6} \left(\frac{m^2}{T^2}\right)^{3/2} + \dots$) has been used to obtain the simple results in Eq. (6). The thermal correction to the coupling λ_S is also omitted. Under these approximations, one can get $e \sim \sum_i h_i^3 + (3\lambda_S)^{3/2}$ and $c \sim \lambda_S/4 + \sum_i h_i^2/12$. To obtain a strong FOPT, one needs $\sigma(T_c)/T_c \gtrsim 1$ as shown in Fig. 3; namely, one must have

$$\frac{\sigma(T_c)}{T_c} \sim \frac{e}{6\pi\lambda_S} \gtrsim 1, \quad (7)$$

where

$$T_c \sim \frac{6\pi\mu_S\sqrt{2\lambda_S}}{\sqrt{-e^2 + 72c\pi^2\lambda_S}}. \quad (8)$$

The parameter spaces in the blue region of Fig. 3 are excluded by the condition of the strong FOPT.

At the end of the FOPT, the χ particles are packed into the so-called Q-balls, which are compact nontopological soliton objects that exist in some new physics models possessing a global symmetry. In this work, we consider the Friedberg-Lee-Sirlin-type Q-balls [6–8] and study whether this type of Q-ball can be given the observed DM density in this scenario. Here, the Q-balls are generated because the χ particles just have global $U(1)$ symmetry¹ $\chi \rightarrow e^{i\alpha}\chi$. The stable Q-ball is a spherical object, where $S = \sigma$ outside the Q-balls and $S = 0$ inside the Q-balls, respectively. To explain the observed DM energy density, it needs to satisfy the condition

¹To avoid the domain wall problem, we assume the Z_2 symmetry is broken.

$$\rho_{\text{DM}} = m_Q n_Q, \quad (9)$$

where the current DM mass density $\rho_{\text{DM}} \simeq 1 \times 10^{-6} \text{ GeV} \cdot \text{cm}^{-3}$. To obtain the Q-ball mass m_Q , it is necessary to minimize the following Q-ball energy²:

$$E(R) = \frac{\pi Q}{R} + \frac{4\pi}{3} R^3 U_0, \quad (10)$$

where $U_0 = \lambda_S \sigma^4 / 4$. And by minimizing Eq. (10), the Q-ball mass can be written as [5]

$$m_Q = \frac{4\sqrt{2}\pi}{3} Q^{3/4} U_0^{1/4}. \quad (11)$$

The stability of the Q-balls needs $m_Q < Q k_1 \sigma$. Since the nonthermal decays of the heavy particles give $n_\chi = n_{\chi^*} = n_B$, one can see that

$$\frac{n_Q Q}{s} = 2 \frac{n_B}{s} = 2\eta_B, \quad (12)$$

where $\eta_B \sim 10^{-10}$. From Eqs. (9) and (12), we obtain

$$\left. \frac{Q}{m_Q} \right|_{t_0} = \frac{2\eta_B s_0}{\rho_{\text{DM}}}, \quad (13)$$

where the t_0 and s_0 represent the present value and the current entropy density $s_0 \simeq 3000 \text{ cm}^{-3}$. Thus, it is necessary to calculate the number density of Q-balls and the typical Q-ball charge at T_* , which can be obtained by estimating the volume V_* from which χ particles are collected into a single Q-ball. Based on the fact that the Q-ball volume is the same order as the volume of the remnant of the symmetry unbroken phase, the radius R_* of the remnant can be estimated by requiring $R_*^3 \Gamma(T) \frac{R_*}{v_b} \sim 1$ for the bubble expansion with velocity v_b [5].

In other words, $R_* \sim (\frac{v_b}{\Gamma(T)})^{1/4}$. Thus, the Q-ball volume is approximately $V_* = \frac{4\pi}{3} R_*^3$, and the number density of Q-balls $n_Q = V_*^{-1}$ at T_* when the phase transition terminates. From Eq. (11), we can calculate the Q-ball mass.

To clearly see the constraints, we need to know the phase transition dynamics from the previous results. It is necessary to start with the calculation of the bubble nucleation rate per unit volume $\Gamma = \Gamma_0(T) e^{-S_E(T)}$ and $\Gamma_0(T) \propto T^4$ [14]. The Euclidean action $S_E(T) \simeq S_3(T)/T$ [15,16], and then $\Gamma = \Gamma_0 e^{-S_3/T}$ [14], where

$$S_3(T) = \int d^3x \left[\frac{1}{2} (\nabla S)^2 + V_{\text{eff}}(S, T) \right]. \quad (14)$$

²Here, we omit the surface energy of the Q-balls since the surface energy is much smaller compared to $E(R)$ [9].

From Eq. (6), the analytic result of S_3/T can be obtained [17,18] as

$$\frac{S_3}{T} \approx \frac{13.72 \times 144\pi^2}{e^2} \left(\frac{-\mu_S^2 + cT^2}{2T^2} \right)^{3/2} f \left[\frac{-\mu_S^2 + cT^2}{2T^2} \frac{144\pi^2 \lambda_S}{e^2} \right] \quad (15)$$

without assuming the thin wall approximation. Here, $f(x) = 1 + \frac{x}{4} \left[1 + \frac{2.4}{1-x} + \frac{0.26}{(1-x)^2} \right]$. And the FOPT termination temperature is determined by

$$S_3(T_*)/T_* = 4 \ln(T_*/100 \text{ GeV}) + 137, \quad (16)$$

which means the nucleation probability of one bubble per one horizon volume becomes order 1. This explains why we can estimate the Q-ball volume V_* when the phase transition terminates in the above discussions.

Combing the above results, the conditions for the observed BAU and DM density give

$$\rho_{\text{DM}}^4 v_b^{3/4} = 73.5 (2\eta_B s_0)^3 \lambda_S \sigma^4 \Gamma^{3/4}. \quad (17)$$

This equation can give explicit constraints on the model parameters, since $\Gamma(T_*)$ is determined by the phase transition dynamics that can be calculated from the original Lagrangian. As for the bubble wall velocity v_b , in principle, it is also depends on the phase transition dynamics. However, we just take $v_b = 0.3$ as the default bubble wall velocity for simplicity. For Eq. (17) to satisfy the current DM density, the BAU, and the condition for strong FOPT, the critical temperature T_c is numerically around several TeV, or roughly $1 \text{ TeV} < T_c < 20 \text{ TeV}$. And k_1 is about $\mathcal{O}(4)$ from Eqs. (5) and (17). We list some benchmark points in Table I.

Here, there is a strong FOPT at several TeV scale, which produces sizable phase transition GWs. We consider three phase transition GW sources: the well-known bubble collisions [19], the turbulence in the fluid, where a certain fraction of the bubble wall energy is converted into turbulence [20,21], and the new source of sound waves [22]. There are usually four parameters that determine the phase transition GW spectrum, namely, v_b , λ_i , α , and $\frac{\beta}{H_*}$. The bubble wall velocity v_b and the energy efficiency factor λ_i ($i = \text{co, tu, sw}$) are not easy to be obtained directly from the Lagrangian, and we just choose some default value or

TABLE I. The benchmark sets after considering the combined constraints for producing the observed DM density and BAU with $v_b = 0.3$.

Benchmark sets	λ_S	e	c	T_c [TeV]	$\frac{\alpha}{T_c}$
I	0.008	0.754	1	15.9	5
II	0.0016	0.151	1	6.6	5

formulas in this work. The parameters α and $\frac{\beta}{H_*}$ can be directly calculated from the above formulas. First, the parameter $\alpha \equiv \frac{\epsilon(T_*)}{\rho_{\text{rad}}(T_*)}$ is defined at the temperature T_* by Eq. (16), wherein $\rho_{\text{rad}}(T_*) = \frac{\pi^2}{30} g_*(T) T^4$ is the plasma thermal energy density and $\epsilon(T_*) = [T \frac{dV_{\text{eff}}^{\text{min}}}{dT} - V_{\text{eff}}^{\text{min}}(T)]|_{T=T_*}$ is the false vacuum energy density. A larger α means a stronger FOPT since the strength of the FOPT is measured by the parameter α . Secondly, the parameter $\frac{\beta}{H_*}$ is defined as $\frac{\beta}{H_*} \equiv T \frac{d(S_3/T)}{dT}|_{T=T_*}$, and β^{-1} represents the typical time duration of the phase transition. After the four parameters are obtained, we can directly calculate the GW spectra from the previous three sources including the redshift effects $\frac{a_*}{a_0} = 1.65 \times 10^{-5} \text{ Hz} \times \frac{1}{H_*} (\frac{T_*}{100 \text{ GeV}}) (\frac{g_*^t}{100})^{1/6}$. Thus, the peak frequency at the current epoch from the three sources can be written as $f_i = f_i^* a_*/a_0$. For the bubble collision, the corresponding $f_{\text{co}}^* = 0.62\beta/(1.8 - 0.1v_b + v_b^2)$ [23] and the phase transition GW spectrum can be written as [23,24]

$$\Omega_{\text{co}}(f)h^2 \approx 1.67 \times 10^{-5} \left(\frac{H_*}{\beta}\right)^2 \left(\frac{\lambda_{\text{co}}\alpha}{1+\alpha}\right)^2 \left(\frac{100}{g_*^t}\right)^{\frac{1}{3}} \times \left(\frac{0.11v_b^3}{0.42+v_b^3}\right) \left[\frac{3.8(f/f_{\text{co}})^{2.8}}{1+2.8(f/f_{\text{co}})^{3.8}}\right]. \quad (18)$$

For the sound wave, the phase transition GW spectrum can be expressed as [22,25]

$$\Omega_{\text{sw}}(f)h^2 \approx 2.65 \times 10^{-6} \left(\frac{H_*}{\beta}\right) \left(\frac{\lambda_{\text{sw}}\alpha}{1+\alpha}\right)^2 \left(\frac{100}{g_*^t}\right)^{\frac{1}{3}} v_b \times \left[\frac{7(f/f_{\text{sw}})^{6/7}}{4+3(f/f_{\text{sw}})^2}\right]^{7/2}$$

with $f_{\text{sw}}^* = 2\beta/(\sqrt{3}v_b)$ at T_* [22,25], and for relativistic bubbles [26] $\lambda_{\text{sw}} \approx \alpha(0.73 + 0.083\sqrt{\alpha} + \alpha)^{-1}$. For the turbulence, the peak frequency at T_* is about $f_{\text{tu}}^* = 1.75\beta/v_b$ [25], and the GW spectrum is formulated by [21,27]

$$\Omega_{\text{tu}}(f)h^2 \approx 3.35 \times 10^{-4} \left(\frac{H_*}{\beta}\right) \left(\frac{\lambda_{\text{tu}}\alpha}{1+\alpha}\right)^{3/2} \left(\frac{100}{g_*^t}\right)^{\frac{1}{3}} v_b \times \frac{(f/f_{\text{tu}})^3}{(1+f/f_{\text{tu}})^{11/3}(1+8\pi f a_0/(a_* H_*))}.$$

In Figs. 4 and 5, we show the GW spectra for the benchmark sets I and II, respectively. And in each figure, (a)–(c) represent the GW spectrum from bubble collision, sound waves, and turbulence, respectively. We can see that the peak frequency ranges from 20 to several hundred Hz. The large peak frequency comes from high critical temperature and large β , which can be seen from the above GW formulas. The peak frequencies are just within the region of

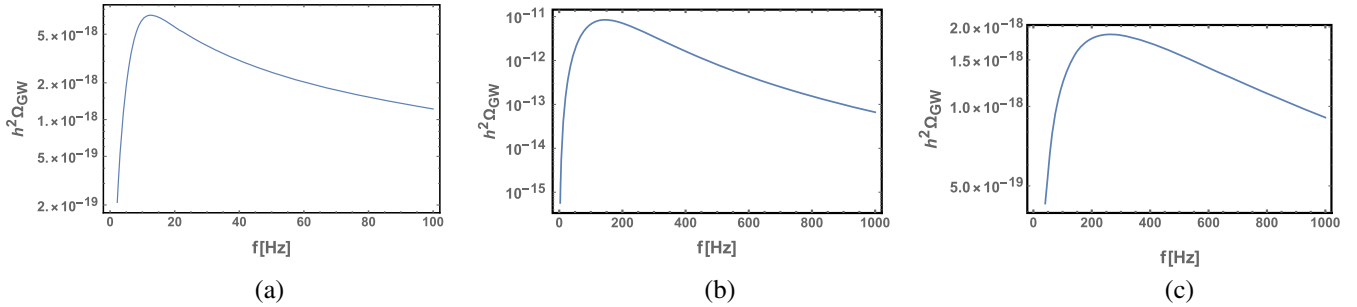


FIG. 4. The predicted GW spectrum for benchmark I with $v_b = 0.3$. Figures (a)–(c) represent the GW spectrum from bubble collision, sound waves, and turbulence, respectively.

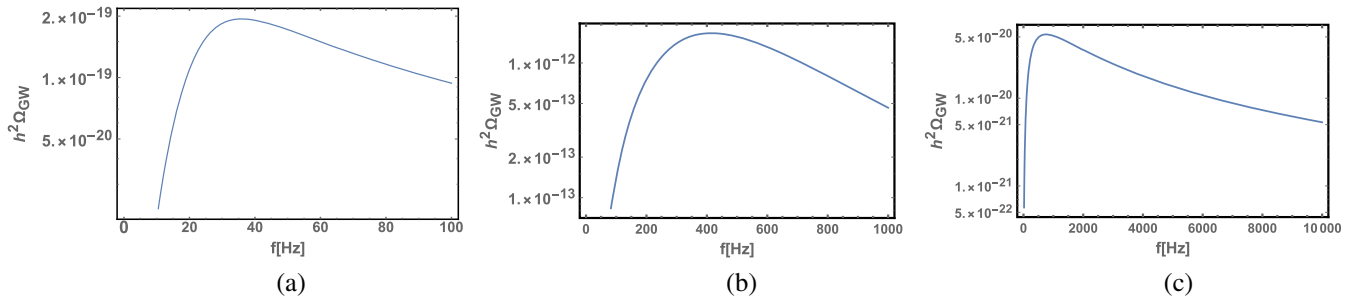


FIG. 5. The predicted GW spectrum for benchmark II with $v_b = 0.3$. Figures (a)–(c) represent the GW spectrum from bubble collision, sound waves, and turbulence, respectively.

aLIGO, but the amplitude of the signal is too weak to be detected by current aLIGO. Future aLIGO-like GW experiments with even higher precision may help to probe this type of GW signal.

IV. COLLIDER PHENOMENOLOGY

Besides the GW signals discussed above, we begin to discuss the collider phenomenology at the LHC in this section. From the Lagrangian in Eq. (1), there are many types of combinations for the up-type quark and down-type quark, which result in abundant collider phenomenology at the LHC. The interactions between quarks and heavy Dirac fermionic mediator X_a can be described by effective operators

$$\mathcal{O}^{dud} = -\frac{\lambda_a^{dud}}{\Lambda^2} (\bar{X}_a P_R d) (\bar{u}^C P_R d), \quad (19)$$

$$\mathcal{O}^{dus} = -\frac{\lambda_a^{dus}}{\Lambda^2} (\bar{X}_a P_R d) (\bar{u}^C P_R s), \quad (20)$$

$$\mathcal{O}^{dub} = -\frac{\lambda_a^{dub}}{\Lambda^2} (\bar{X}_a P_R d) (\bar{u}^C P_R b), \quad (21)$$

$$\mathcal{O}^{dtd} = -\frac{\lambda_a^{dtd}}{\Lambda^2} (\bar{X}_a P_R d) (\bar{t}^C P_R d). \quad (22)$$

At tree level, these operators can result in the following processes,

$$u(p_1) + d(p_2) \rightarrow \bar{d}(p_3) + X_a(p_4), \quad (23)$$

$$u(p_1) + d(p_2) \rightarrow \bar{s}(p_3) + X_a(p_4), \quad (24)$$

$$u(p_1) + d(p_2) \rightarrow \bar{b}(p_3) + X_a(p_4), \quad (25)$$

$$d(p_1) + d(p_2) \rightarrow \bar{t}(p_3) + X_a(p_4), \quad (26)$$

and their various crossings and charge-conjugated processes. The dominant decay channel of X_a is $X_a \rightarrow Y\bar{\chi}\chi$, and X_a behaves as the missing energy in the detector. The subdominant process of four jet (X_a can decay to three quarks) is not discussed in this work. Similar collider signals are discussed using LHC Run-I data in Ref. [11] at tree level. So the interactions can be explored by performing monojet and monotop analysis at the LHC. Because the LHC is a proton-proton collider with high precision, the QCD NLO predictions for these processes are necessary in order to obtain reliable results. In this section, we calculate the NLO QCD corrections for all of the above processes, and investigate the constraints on the interactions described by Eq. (19). For convenience, when there is no special description, the new physics scale Λ is fixed at 5 TeV and the dimensionless coupling λ_{dqg} is set as 1. Here, the parton distribution function (PDF) NNPDF30nlo [28] is used and

top-quark mass is fixed at 173 GeV. To compare with the parameter spaces allowed by the conditions of successful baryogenesis and DM, we just need to rescale these parameters.

A. NLO QCD calculations

The NLO QCD correction can be expressed as

$$\sigma_{\text{NLO}} = \sigma_R + \sigma_V = \int d\Gamma_3 |\mathcal{M}_{2 \rightarrow 3}|^2 + \int d\Gamma_2 |\mathcal{M}_{2 \rightarrow 2}|^2, \quad (27)$$

where $d\Gamma_n$ denotes n -body phase space. By two cutoff phase space slicing method [29], the real radiation in σ_R can be divided into soft, collinear, and hard regions

$$\sigma_R = \sigma_S + \sigma_C + \sigma_H, \quad (28)$$

where $\sigma_{S,C,H}$ depend on two cutoff parameters δ_s and δ_c . With dimension regularization, the hard contribution is finite, which can be calculated numerically. While σ_S and σ_C suffer from soft and collinear divergences, which cancel with the infrared (IR) singularity in the virtual correction σ_V . So the sum of all the contributions is IR safe. Using this approach, we first give the analytical results of one-loop virtual correction for monojet and monotop productions in Appendix.

The numerical results of monojet processes induced by \mathcal{O}_{dud} and $\mathcal{O}_{dus(b)}$ are listed in Tables II and III, respectively. The events are selected with jets in region $p_{T,j} > 250$ GeV and $|\eta_j| < 2.4$, which is consistent with the kinematic cuts used in Ref. [30]. The factorization and renormalization scales are fixed at 1 TeV. The cross section of the monojet process induced by \mathcal{O}_{dud} is significantly larger than the one of \mathcal{O}_{dus} because the parton density of the u quark is much larger than the s quark. The K -factor decreases with increasing mass of Dirac fermionic X_a and missing transverse energy cut \bar{E}_T . The differences of the cross section between the processes induced by \mathcal{O}_{dus} and \mathcal{O}_{dub} are very tiny, because b quark mass can be neglected at high energy and the PDFs of strange and bottom quark are much smaller than u and d .

TABLE II. Fixed order results for the monojet process induced by \mathcal{O}_{dud} at the 13 TeV LHC.

m_X [TeV]	$\bar{E}_T > 700$ GeV			$\bar{E}_T > 1$ TeV		
	σ_{LO} [fb]	σ_{NLO} [fb]	K -factor	σ_{LO} [fb]	σ_{NLO} [fb]	K -factor
1.2	5.49	5.63	1.02	3.61	3.64	1.01
2	2.19	2.19	1	1.51	1.49	0.99
2.8	0.766	0.748	0.98	0.54	0.52	0.96
3.6	0.241	0.23	0.076	0.17	0.16	0.94
4	0.13	0.123	0.95	0.091	0.085	0.93

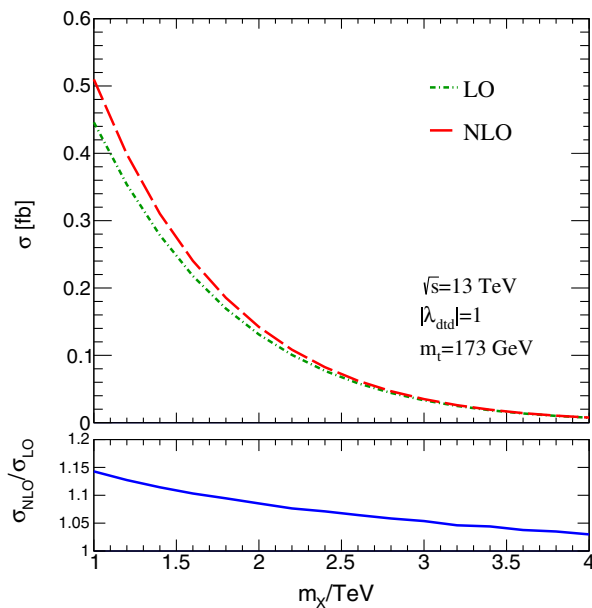
TABLE III. Fixed order results for the monojet process induced by $\mathcal{O}_{dus(b)}$ at the 13 TeV LHC.

m_X [TeV]	$\cancel{E}_T > 700$ GeV			$\cancel{E}_T > 1$ TeV		
	σ_{LO} [fb]	σ_{NLO} [fb]	K -factor	σ_{LO} [fb]	σ_{NLO} [fb]	K -factor
1.2	1.11	1.13	1.02	0.713	0.713	1.00
2	0.463	0.461	0.996	0.318	0.312	0.98
2.8	0.174	0.170	0.974	0.124	0.118	0.957
3.6	0.06	0.057	0.953	0.043	0.04	0.938
4	0.034	0.032	0.944	0.0245	0.0228	0.93

The fixed order result for the monotop process is shown in Fig. 6 up to NLO level. The inclusive cross section decreases from 0.5 to 0.007 fb, and the K -factor also decreases from 1.14 to 1.03 as m_X increases from 1 to 4 TeV. Because the branch ratio of $t \rightarrow b + W(\rightarrow l\nu_l)$, ($l = e, \mu$) is about 20%, we can estimate that the inclusive cross section of monotop signal is less than 0.1 fb. This helps us to discuss the constraints on \mathcal{O}_{did} in the following section.

B. Monojet analysis

The monojet signature has been studied in detail by current experiments [30], where the analysis was performed with an integrated luminosity of 36.1 fb^{-1} at the 13 TeV LHC. Here, the DM signals are simulated by Madgraph5 with parton shower. Events are selected with $E_{\text{miss}}^T > 250$ GeV, where a leading (highest- p_T) jet with $p_T > 250$ GeV and $|\eta| < 2.4$ is required. Most of the SM backgrounds are from $Z(\rightarrow \nu\nu) + \text{jets}$ processes. $W(\rightarrow \tau\nu) + \text{jets}$ processes also give significant contributions. Top pair, diboson, multijet, and single top processes give small contributions. In Ref. [30], the SM background $Z + \text{jets}$


 FIG. 6. Cross section of monotop process induced by \mathcal{O}_{did} at the 13 TeV LHC.

and $W + \text{jets}$ are normalized to next-to-next-to-leading order QCD and NLO electroweak predictions. Other backgrounds are simulated at NLO QCD level by using Monte Carlo (MC) generators Powheg-Box and MadGraph5_aMC@NLO [31]. In Table IV, we extract the monojet background in various signal regions from Ref. [30].

In principle, if no signal is observed, the couplings λ_{dud} and $\lambda_{dus(b)}$ cannot be too large. Thus, in Fig. 7, we give 3σ exclusion limits of the couplings against heavy Dirac fermion mass for integrated luminosity of 100 and 300 fb^{-1} at the 13 TeV LHC by using the NLO theoretical predictions. The colored regions denote the parameters spaces that should be excluded if no signal is observed. The constraint for λ_{dud} is stronger than λ_{dud} because the former cross section is larger.

C. Monotop analysis

Monotop signals can be explored by using hadronic or semileptonic top decay modes [32,33]. For highly boosted monotop production, we can take advantage of the jet substructure technique to perform top reconstruction and suppress the multijet background [34,35]. For the unboosted top, semileptonic can be used due to the clean leptonic signature. In this work, we do analysis with semileptonic top decay modes. The background contributions are mainly from $W + \text{jets}$, single top, top pair, and gauge boson pair productions. Neutrino from W, Z , and top decay results in missing transverse energy. The dominant background is from the $W + \text{jets}$ process because of its huge cross section, so b -tagging must be performed to suppress this background. Here, the backgrounds are generated with 0/1/2 jet parton level matching, based on the default k_T -jet MLM scheme in MadGraph5_aMC@NLO.

First, we introduce the basic cuts

$$p_T^b > 70 \text{ GeV}, \quad |\eta^{b,l}| < 2.4. \quad (29)$$

The selected leptons should be isolated, having $\sum_i p_{T,i}$ less than 10% of its transverse momentum within a cone of $\Delta R = 0.3$ around it.

 TABLE IV. SM background predictions in the signal region for several inclusive \cancel{E}_T selections.

\cancel{E}_T [GeV]	Background [fb]
> 250	7077
> 300	3997
> 350	2128
> 400	1150
> 500	378.9
> 600	141.2
> 700	58.78
> 800	27.15
> 900	12.96
> 1000	6.787

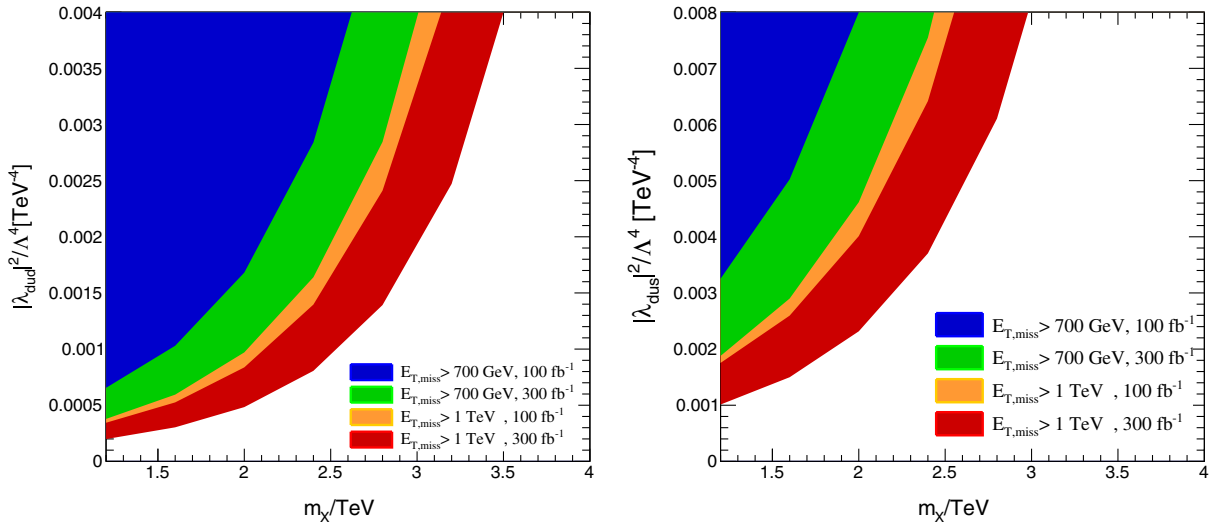


FIG. 7. Constraints on coupling λ_{ijk} and mass m_X by monojet measurements at the 13 TeV LHC.

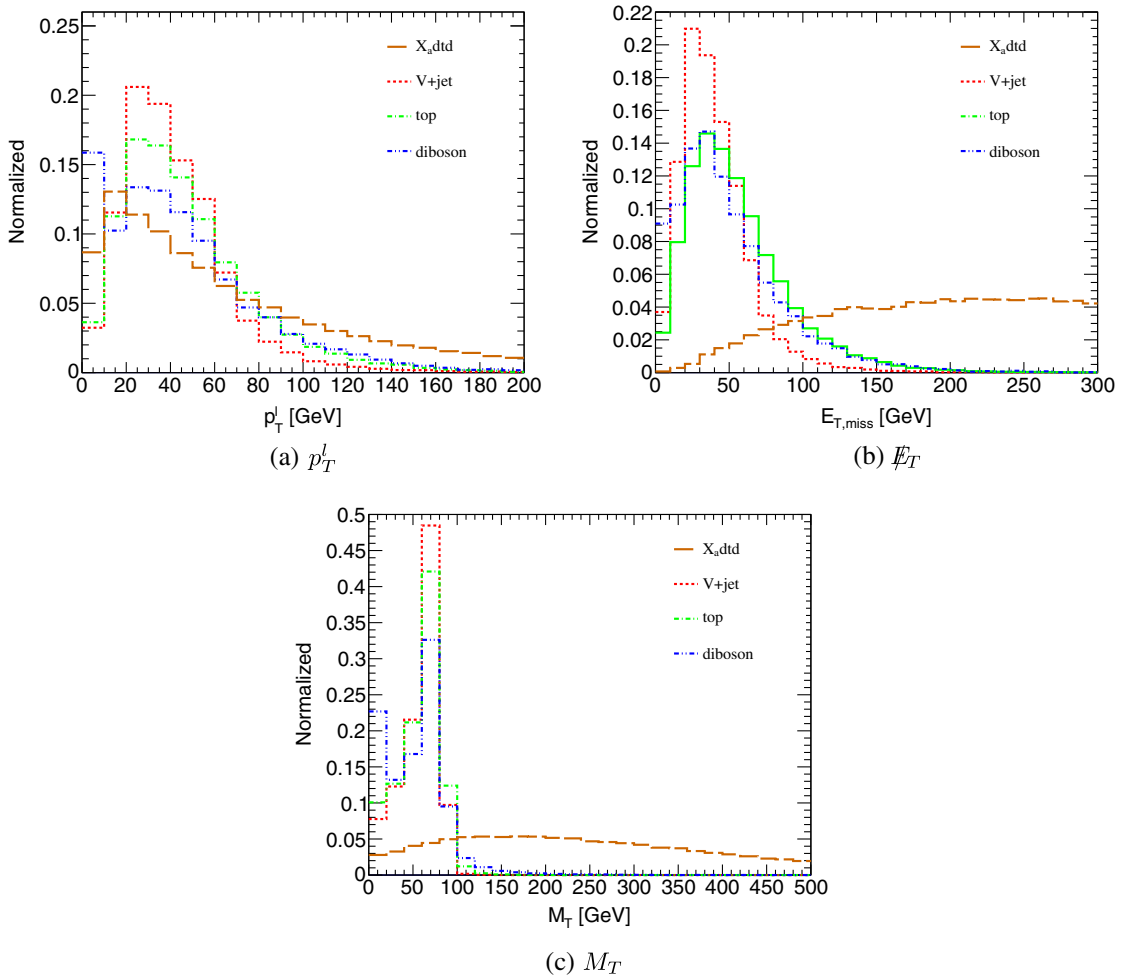


FIG. 8. Normalized spectra for signal and background in monotop searching at the 13 TeV LHC. Top denotes the sum of background for top pair, single top, and associated production of tW .

The normalized transverse momentum distribution of lepton e or μ in the semileptonic mode is shown in Fig. 8(a). There are no significant differences between various backgrounds and signals. So we choose a loose cut

$$p_T^l > 30 \text{ GeV}. \quad (30)$$

In addition, we veto extra lepton e or μ with $p_T^l > 30 \text{ GeV}$ to suppress the background from $pp \rightarrow W(\rightarrow l\nu_l) + W(\rightarrow l\nu_l) + j$, $pp \rightarrow W(\rightarrow l\nu_l) + Z(\rightarrow ll) + j$, and $pp \rightarrow W(\rightarrow l\nu_l) + t(\rightarrow b l\nu_l)$.

Figure 8(b) shows the normalized distribution of the missing transverse energy. The peak of the background spectrum is around $m_W/2 \approx 40 \text{ GeV}$, because the (anti-)neutrino decay from W boson takes half of its energy. The missing energy for signal is significantly larger because two invisible particles are contained. Therefore, the missing transverse energy cut can be chosen as

$$E_T > 100 \text{ GeV}. \quad (31)$$

In Fig. 8(c), we show the normalized transverse mass distribution for background and signal, which is defined with lepton and missing transverse momentum

$$M_T = \sqrt{(E + E_T^l)^2 - (\vec{p}_T + \vec{p}_T^l)^2}. \quad (32)$$

The spectra of various background have a peak around the W boson mass $m_W \approx 80 \text{ GeV}$, because the lepton and neutrino is from W boson decay, while the transverse mass spectrum of signal is smoothly distributed due to the fact that two invisible particles are contained. Therefore, the missing transverse energy cut can be performed as

$$M_T > 100 \text{ GeV}. \quad (33)$$

In order to suppress the huge background of $W + \text{jets}$, the b -tagging technique must be involved. The b -tagging efficiency is chosen as 70%, and the light-jet-to- b mis-tagging probabilities are assumed of 1%. Combining with the improved cuts of p_T^l , E_T , and M_T , the backgrounds of $V + \text{jets}$, top, and diboson are 1.094, 0.455, and 1.05 fb, respectively. The background from the diboson is still significant because of the decay mode $W(\rightarrow l\nu_l)Z(\rightarrow \nu\nu)$. Figure 9 gives the 3σ exclusion limits of the couplings against heavy Dirac fermion mass for integrated luminosity of 100 and 300 fb^{-1} at the 13 TeV LHC by using the NLO theoretical predictions. Comparing with λ_{dud} and λ_{dus} , the constraint is very weak, because the cross section of monoton induced by \mathcal{O}_{dd} is much smaller.

V. CONCLUSION

We have studied the possibility of detecting the mechanism to solve the baryogenesis and DM with various large DM masses through strong first-order phase transition and Q-balls. The signals at GW experiments and the LHC with

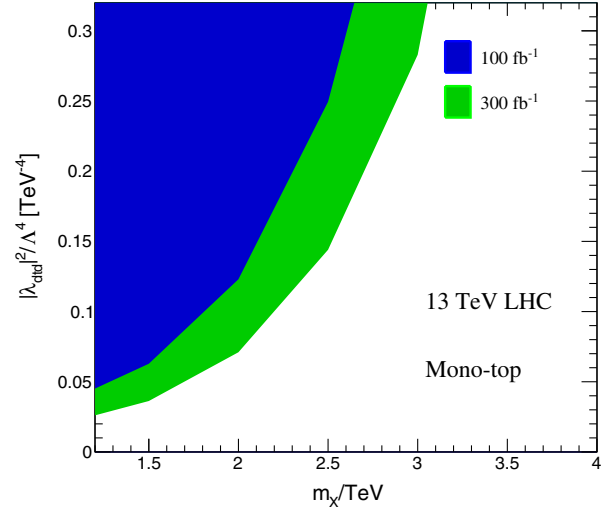


FIG. 9. Normalized spectra for signal and background in monoton searching at the 13 TeV LHC.

QCD NLO accuracy have been discussed in detail. We have found that the GWs could provide a realistic and complementary approach for testing the baryogenesis and DM scenario. Our results show that the phase transition process in the early Universe may play an important role in solving the fundamental problems in particle cosmology. More systematical study on the phase transition physics in particle cosmology is left to our future study.

ACKNOWLEDGMENTS

We deeply appreciate Ze Long Liu's help in accomplishing the complicated QCD loop calculations. F. P. H. thanks David J. Weir for his wonderful lectures on phase transition gravitational waves, and the useful discussions on Q-balls. C. S. L. is supported by the National Nature Science Foundation of China under Grant No. 11375013. F. P. H. is supported by IBS under the project code, IBS-R018-D1.

APPENDIX: ANALYTICAL RESULTS OF NLO QCD CORRECTIONS

The virtual corrections contain both ultraviolet (UV) and IR divergences, and the UV divergences can be canceled by introducing counterterms. For the external fields, we fix all the renormalization constants using on-shell subtraction

$$\begin{aligned} \delta Z_2^q &= -\frac{\alpha_s}{3\pi} C_e \left(\frac{1}{\epsilon_{\text{UV}}} - \frac{1}{\epsilon_{\text{IR}}} \right), \\ \delta Z_2^t &= -\frac{\alpha_s}{3\pi} C_e \left(\frac{1}{\epsilon_{\text{UV}}} + \frac{2}{\epsilon_{\text{IR}}} + 4 + 3 \ln \left(\frac{\mu^2}{m_t^2} \right) \right), \end{aligned} \quad (\text{A1})$$

with $C_e = \frac{(4\pi)^\epsilon}{\Gamma(1-\epsilon)}$. For the coupling constants, we use the $\overline{\text{MS}}$ scheme,

$$\delta Z_{\lambda_{dud}} = \delta Z_{\lambda_{dus(b)}} = \delta Z_{\lambda_{ddd}} = -\frac{\alpha_s}{2\pi} C_\epsilon \frac{1}{\epsilon_{UV}}. \quad (\text{A2})$$

For the operator \mathcal{O}^{dud} , the UV renormalized one-loop virtual QCD correction can be expressed as

$$\begin{aligned} i\mathcal{M}_{ud \rightarrow dX_a}^{\text{virt}} &= i\mathcal{M}_{ud \rightarrow dX_a}^{\text{born}} \times \frac{\alpha_s}{4\pi} C_\epsilon \left\{ -\frac{4}{\epsilon^2} - \frac{2}{3\epsilon} \left[2 \ln \left(-\frac{\mu^2}{s} \right) + 2 \ln \left(-\frac{\mu^2}{t} \right) + 2 \ln \left(-\frac{\mu^2}{u} \right) + 9 \right] \right. \\ &\quad - \frac{2}{3} \left[\ln \left(-\frac{\mu^2}{s} \right)^2 + \ln \left(-\frac{\mu^2}{t} \right)^2 + \ln \left(-\frac{\mu^2}{u} \right)^2 + 2 \ln \left(-\frac{\mu^2}{t} \right) + 4 \ln \left(-\frac{\mu^2}{u} \right) \right. \\ &\quad \left. \left. + \frac{2(m_X^2(2t-s) + s^2 + st - 2t^2)}{m_X^2(s+t) - (s-t)^2} \ln \left(-\frac{t}{s} \right) + 14 \right] \right\}. \quad (\text{A3}) \end{aligned}$$

For the operators \mathcal{O}^{dus} and \mathcal{O}^{dub} , the UV renormalized one-loop virtual QCD correction can be expressed as

$$\begin{aligned} i\mathcal{M}_{us \rightarrow dX_a}^{\text{virt}} &= i\mathcal{M}_{us \rightarrow dX_a}^{\text{born}} \times \frac{\alpha_s}{4\pi} C_\epsilon \left\{ -\frac{4}{\epsilon^2} - \frac{2}{3\epsilon} \left[2 \ln \left(-\frac{\mu^2}{s} \right) + 2 \ln \left(-\frac{\mu^2}{t} \right) + 2 \ln \left(-\frac{\mu^2}{u} \right) + 9 \right] \right. \\ &\quad \left. - \frac{2}{3} \left[\ln \left(-\frac{\mu^2}{s} \right)^2 + \ln \left(-\frac{\mu^2}{t} \right)^2 + \ln \left(-\frac{\mu^2}{u} \right)^2 + 6 \ln \left(-\frac{\mu^2}{t} \right) - \frac{2(m_X^2 - s + t)}{s - m_X^2} \ln \left(\frac{t}{u} \right) + 14 \right] \right\}. \quad (\text{A4}) \end{aligned}$$

For the operator \mathcal{O}^{did} , the UV renormalized one-loop virtual QCD correction can be expressed as

$$\begin{aligned} i\mathcal{M}_{dd \rightarrow tX_a}^{\text{virt}} &= i\mathcal{M}_{dd \rightarrow tX_a}^{\text{born}} \times \frac{\alpha_s}{4\pi} C_\epsilon \left\{ \frac{8}{-3\epsilon^2} - \frac{4}{3\epsilon} \left[\log \left(-\frac{\mu^2}{s} \right) + \log \left(\frac{\mu^2}{m_t^2} \right) + \log \left(\frac{m_t^2}{m_t^2 - u} \right) \right. \right. \\ &\quad \left. \left. + \log \left(\frac{m_t^2}{m_t^2 - t} \right) \right] - \frac{2}{3} \log^2 \left(\frac{\mu^2}{m_t^2} \right) - \frac{2}{3} \log^2 \left(-\frac{\mu^2}{s} \right) - \frac{8}{3} \log \left(-\frac{\mu^2}{s} \right) \right. \\ &\quad \left. - \frac{2}{3} \log \left(\frac{\mu^2}{m_t^2} \right) \left[2 \log \left(-\frac{m_t^2}{m_X^2 - s - t} \right) + 2 \log \left(\frac{m_t^2}{m_t^2 - t} \right) + 1 \right] \right. \\ &\quad \left. - \frac{2}{3} \log^2 \left(-\frac{m_t^2}{m_X^2 - s - t} \right) - \frac{4}{3} \log^2 \left(\frac{m_t^2}{m_t^2 - t} \right) \right. \\ &\quad \left. - \frac{4}{3} \log \left(\frac{m_t^2}{m_t^2 - t} \right) \frac{(2m_t^4(m_X^2 - t) + m_t^2 s(m_X^2 - 2t) + t(-2m_X^2(s+t) + 2s^2 + 5st + 2t^2))}{t(m_t^2(4m_X^2 - s - 4t) - m_X^2(s+4t) + (s+2t)^2)} \right. \\ &\quad \left. - \frac{4}{3} \log \left(-\frac{m_t^2}{m_X^2 - s - t} \right) \left[\frac{m_t^4(4m_X^2 - s - 4t) + m_t^2(2m_X^4 - m_X^2(s+8t) + 2t(2s+3t))}{(m_t^2 + m_X^2 - s - t)(m_t^2(4m_X^2 - s - 4t) - m_X^2(s+4t) + (s+2t)^2)} \right. \right. \\ &\quad \left. \left. + \frac{m_X^4(s-2t) - 2m_X^2(s^2 - 2t^2) + s^3 + 2s^2t - st^2 - 2t^3}{(m_t^2 + m_X^2 - s - t)(m_t^2(4m_X^2 - s - 4t) - m_X^2(s+4t) + (s+2t)^2)} \right] \right. \\ &\quad \left. - \frac{2}{9} \left[-6\text{Li}_2 \left(\frac{m_t^2 + m_X^2 - s - t}{m_X^2 - s - t} \right) - 6\text{Li}_2 \left(-\frac{t}{m_t^2 - t} \right) + \pi^2 + 33 \right] \right\}. \end{aligned}$$

[1] P. A. R. Ade *et al.* (Planck Collaboration), *Astron. Astrophys.* **571**, A16 (2014).

[2] C. Patrignani *et al.* (Particle Data Group), *Chin. Phys. C* **40**, 100001 (2016).

[3] A. D. Sakharov, *Usp. Fiz. Nauk* **161**, 61 (1991) [*Pis'ma Zh. Eksp. Teor. Fiz.* **5**, 32 (1967)].

[4] M. Dine and A. Kusenko, *Rev. Mod. Phys.* **76**, 1 (2003).

[5] E. Krylov, A. Levin, and V. Rubakov, *Phys. Rev. D* **87**, 083528 (2013).

[6] R. Friedberg, T. D. Lee, and A. Sirlin, *Nucl. Phys.* **B115**, 1 (1976).

- [7] R. Friedberg, T. D. Lee, and A. Sirlin, *Phys. Rev. D* **13**, 2739 (1976).
- [8] R. Friedberg, T. D. Lee, and A. Sirlin, *Nucl. Phys.* **B115**, 32 (1976).
- [9] B. Shuve and C. Tamarit, *J. High Energy Phys.* **10** (2017) 122.
- [10] B. P. Abbott *et al.* (Virgo, LIGO Scientific Collaborations), *Phys. Rev. Lett.* **116**, 061102 (2016).
- [11] S. V. Demidov, D. S. Gorbunov, and D. V. Kirpichnikov, *Phys. Rev. D* **91**, 035005 (2015).
- [12] H. Davoudiasl, D. E. Morrissey, K. Sigurdson, and S. Tulin, *Phys. Rev. Lett.* **105**, 211304 (2010).
- [13] M. Quiros, in *Proceedings, Summer School in High-Energy Physics and Cosmology, Trieste, Italy, June 29–July 17, 1998* (1999), pp. 187–259.
- [14] A. D. Linde, *Nucl. Phys.* **B216**, 421 (1983); **B223**, 544(E) (1983).
- [15] S. R. Coleman, *Phys. Rev. D* **15**, 2929 (1977); **16**, 1248(E) (1977).
- [16] C. G. Callan, Jr. and S. R. Coleman, *Phys. Rev. D* **16**, 1762 (1977).
- [17] M. Dine, R. G. Leigh, P. Y. Huet, A. D. Linde, and D. A. Linde, *Phys. Rev. D* **46**, 550 (1992).
- [18] M. Dine, R. G. Leigh, P. Huet, A. D. Linde, and D. A. Linde, *Phys. Lett. B* **283**, 319 (1992).
- [19] M. Kamionkowski, A. Kosowsky, and M. S. Turner, *Phys. Rev. D* **49**, 2837 (1994).
- [20] A. Kosowsky, A. Mack, and T. Kahnashvili, *Phys. Rev. D* **66**, 024030 (2002).
- [21] C. Caprini, R. Durrer, and G. Servant, *J. Cosmol. Astropart. Phys.* **12** (2009) 024.
- [22] M. Hindmarsh, S. J. Huber, K. Rummukainen, and D. J. Weir, *Phys. Rev. Lett.* **112**, 041301 (2014).
- [23] S. J. Huber and T. Konstandin, *J. Cosmol. Astropart. Phys.* **09** (2008) 022.
- [24] R. Jinno and M. Takimoto, *Phys. Rev. D* **95**, 024009 (2017).
- [25] C. Caprini *et al.*, *J. Cosmol. Astropart. Phys.* **04** (2016) 001.
- [26] J. R. Espinosa, T. Konstandin, J. M. No, and G. Servant, *J. Cosmol. Astropart. Phys.* **06** (2010) 028.
- [27] P. Binetruy, A. Bohe, C. Caprini, and J.-F. Dufaux, *J. Cosmol. Astropart. Phys.* **06** (2012) 027.
- [28] R. D. Ball *et al.* (NNPDF Collaboration), *J. High Energy Phys.* **04** (2015) 040.
- [29] B. W. Harris and J. F. Owens, *Phys. Rev. D* **65**, 094032 (2002).
- [30] T. A. collaboration (ATLAS), Report No. ATLAS-CONF-2017-060, 2017.
- [31] J. Alwall, R. Frederix, S. Frixione, V. Hirschi, F. Maltoni, O. Mattelaer, H. S. Shao, T. Stelzer, P. Torrielli, and M. Zaro, *J. High Energy Phys.* **07** (2014) 079.
- [32] J. Andrea, B. Fuks, and F. Maltoni, *Phys. Rev. D* **84**, 074025 (2011).
- [33] J. Wang, C. S. Li, D. Y. Shao, and H. Zhang, *Phys. Rev. D* **86**, 034008 (2012).
- [34] C. Collaboration (CMS), Report No. CMS-PAS-EXO-16-040, 2016.
- [35] C. Collaboration (CMS), Report No. CMS-PAS-EXO-16-051, 2017.